CHAPTER
FOUR

HEAT TRANSFER AND MIXING CHARACTERISTICS OF TWO-DIMENSIONAL TURBULENT CONFINED IMPINGING STREAMS

A mathematician knows how to solve a
problem – but he can't do it
W.E. Milne

4.1. INTRODUCTION

As mentioned in the previous chapters impinging streams (IS) provide a relatively new flow configuration that has proved useful in conducting a wide range of chemical engineering unit operations. A number of publications, as partially reviewed in Chapter 2, have reported applications of this flow configuration in such operations as absorption (Berman et al., 2000a,b), catalytic reactions (Sohrabi and Marvast, 2000), drying (Kitron and Tamir, 1988; Kudra and Mujumdar, 1989; Kudra and Mujumdar, 1995), dust collection (Berman and Tamir, 1996), liquid-liquid extraction (Berman and Tamir, 2000) as well as mixing (Tamir, 1994; Hosseinalipour and Mujumdar, 1997a,b; Unger et al., 1998). These papers, however, are based exclusively upon experimental results or else are limited to processes conducted in the laminar flow regime. Very few papers (e.g., Hosseinalipour and Mujumdar, 1995) have attempted modeling of turbulent transport processes in this flow configuration.

A number of papers have recently been published on modeling of turbulent flow and heat transfer behavior of impinging jets (IJ), which display characteristics somewhat similar to those of impinging streams. Seyedein et al. (1994) used both low-Reynolds

and high-Reynolds number versions of *k*-ε turbulence model to predict the flow field and heat transfer impingement due to a turbulent single headed slot jet discharging normally into a confined two-dimensional channel. Better agreement between numerical results obtained using low-Reynolds number models and the available experimental data is noted compared to those results obtained using high-Reynolds number model. Hosseinalipour and Mujumdar (1995) used five different versions of the low-Reynolds number *k*-ε models and the standard high-Reynolds number model to study the fluid flow and heat transfer characteristics of two-dimensional turbulent confined impinging and opposing jets flows. A so-called "Yap correction" was also tested with low-Reynolds number models to investigate its effect on the heat transfer predictions for the impinging jet case. Experimental data and numerical predictions by different turbulence models were compared for the turbulent impinging jet. Due to lack of experimental data, however, only the numerical results of the opposing jet case were presented. Morris et al. (1996) modified the converged solution obtained from commercial finite-volume code via the application of different turbulent Prandtl number functions in their post-processing program. Their predicted heat transfer results were then compared with selected experimental data; the predicted stagnation and average heat transfer coefficients agree with experiments to within a maximum deviation of 16-20 percent. To avoid using a full second moment closure, which may be a solution to modeling the flow with recirculation and streamline curvature, some investigators have recently employed simplified models which combine computational robustness and efficiency of the linear eddy viscosity models (e.g., *k*-ε models) with the improved model accuracy of second moment closures (e.g., Behnia et al., 1999; Bauer et al., 2000).

In this chapter a new composite turbulence model is proposed and applied to study thermal mixing of turbulent confined impinging streams. The model consists of a low-Reynolds number *k*-ε model, Yap correction as well as a formula for the turbulent (eddy) viscosity, which is incorporated directly into the computational fluid dynamic code. Experiments were conducted to verify the numerical results obtained using this model. The numerical results were also compared with experimental impingement heat transfer data available in the literature. Good agreement between the numerical and experimental data is noted for both impinging streams and impingement flows. The

model was then used to study the effects of various operating as well as geometric parameters on thermal mixing of two-dimensional turbulent confined impinging streams. It is found that the mixing behavior of turbulent confined impinging streams is quite different from that of laminar IS reported in Chapter 3. An explanation of the difference, based on results presented in this chapter and the previous one, is given.

4.2. EXPERIMENTAL SET-UP AND PROCEDURE

A schematic diagram of the overall heat transfer experimental set-up is shown in Figure 4.1a. Air was supplied by a blower (model no. 6350B-2, Wainbee Ltd., Pointe Claire, QC) and the flowrate in each flow branch was controlled by means of gate valves. One of the air streams was heated to pre-selected temperatures (either 10^{o} or 20^{o} C above the ambient) by an electric heater rated at 2.5 kW (model no. KSEF-30/120, Omega Engineering, Inc., Stamford, CT), which was controlled by a PID controller (model no. CN76000, Omega Engineering, Inc., Stamford, CT). The other air stream was left at ambient conditions. The air flowrate in each flow branch was measured using a pre-calibrated pitot tube (model no. FPT-6130, Omega Engineering, Inc., Stamford, CT). Differential pressure drop across the pitot tube was measured using a manometer filled with a manometric fluid (Red Gage Oil 0.826 SG, Dwyer Instruments, Inc., Michigan City, IN).

The air streams were then fed into the IS through two inlets (see Figure 4.1b). The two streams impinged normally against each other and left the IS through the exits situated symmetrically on either side of the impingement region. Temperature distributions in the IS were measured using 32 type K thermocouples (model no. EXFF-K-20-SLE, Omega Engineering, Inc., Stamford, CT; AWG no. 20), which were permanently mounted across the exit channel (see Figure 4.1c) and connected to an expansion board (model no. EXP-32, Omega Engineering, Inc., Stamford, CT). Thermocouple signals were multiplexed to a data acquisition card (model no. CIO-DAS16Jr, Omega Engineering, Inc., Stamford, CT) installed in a PC. LABTECH NOTEBOOK software (version 10.0.2, Laboratory Technologies Corp., Wilmington, MA) was used to read and record the temperature data for subsequent analyses. To test

whether these thermocouples had any effect on mixing of impinging streams two sets of experiments were conducted. In the first set of experiment only one thermocouple was used at a time while 32 thermocouples were used simultaneously in the second set of experiment. The maximum difference in temperature values at the same measuring locations obtained from these two sets of experiments was less than 5%. This indicates that the presence of thermocouples does not have significant effect on mixing of impinging streams. Experiments were also conducted to determine the effect of the third dimension (z dimension, which equals to 2.5 cm) on the thermal characteristics of the system. A maximum difference of 4.5% was noted between the temperature values measured at the middle plane (50% of 2.5 cm) and at the quarter (25% of 2.5 cm) of the z dimension. This justifies the two-dimensionality assumption used in the present study.

Photographs of the overall heat transfer experimental set-up and of the IS used in the heat transfer experiments are shown in Figures 4.1d and 4.1e, respectively.

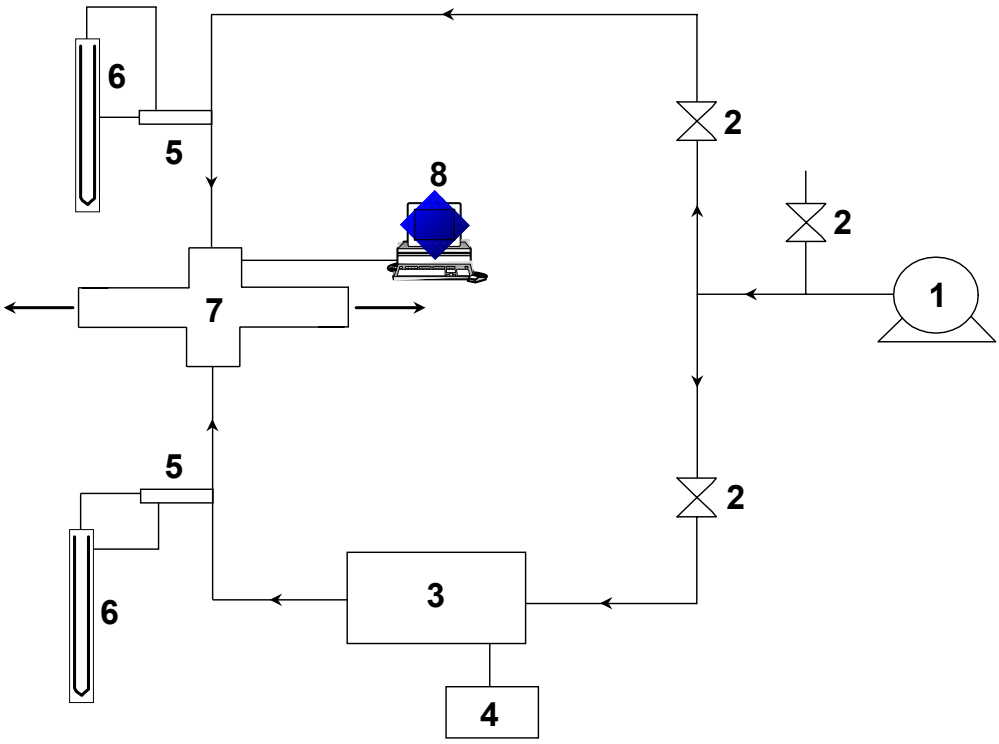

Figure 4.1a. A schematic diagram of the overall heat transfer experimental set-up
1: air blower; 2: gate valves; 3: heater; 4: controller; 5: pitot tubes; 6: manometers; 7: IS; 8: computer and data acquisition system

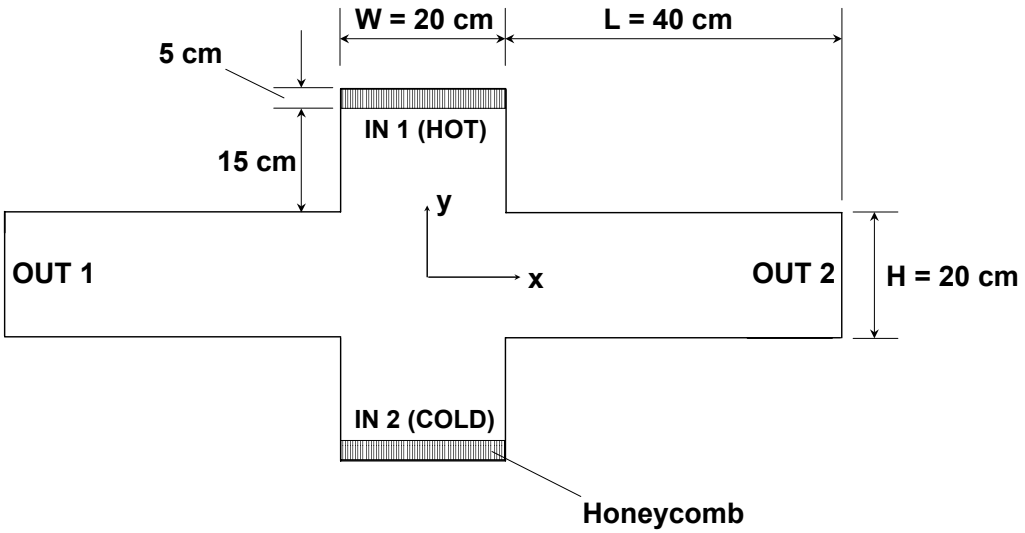

Figure 4.1b. Detailed diagram of the IS used in the heat transfer experiments

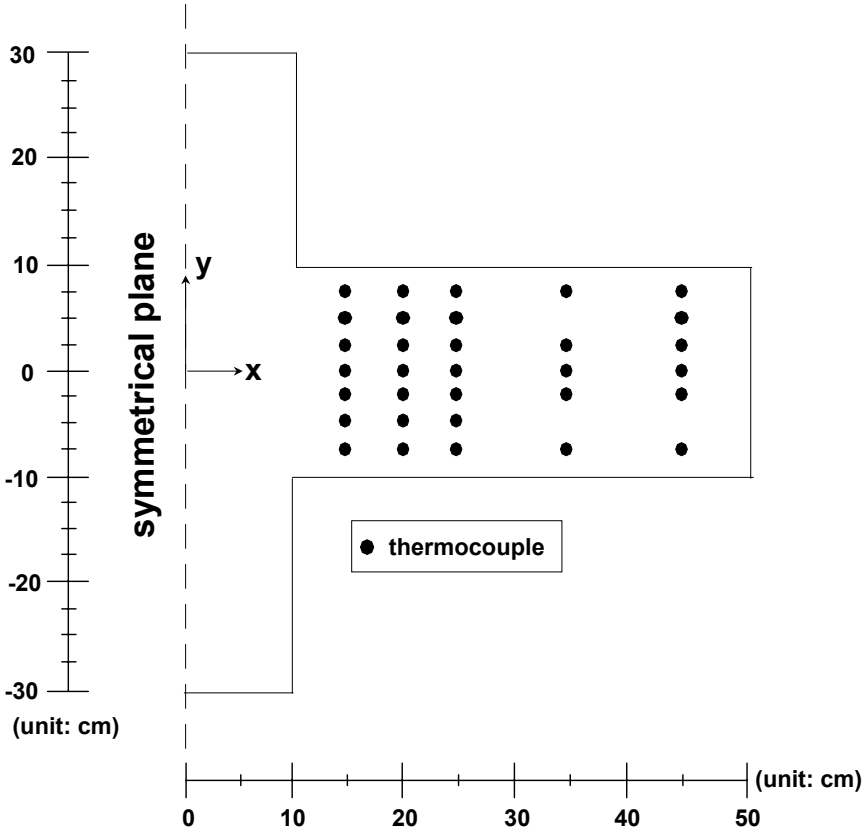

Figure 4.1c. Locations of thermocouples used in the heat transfer experiments

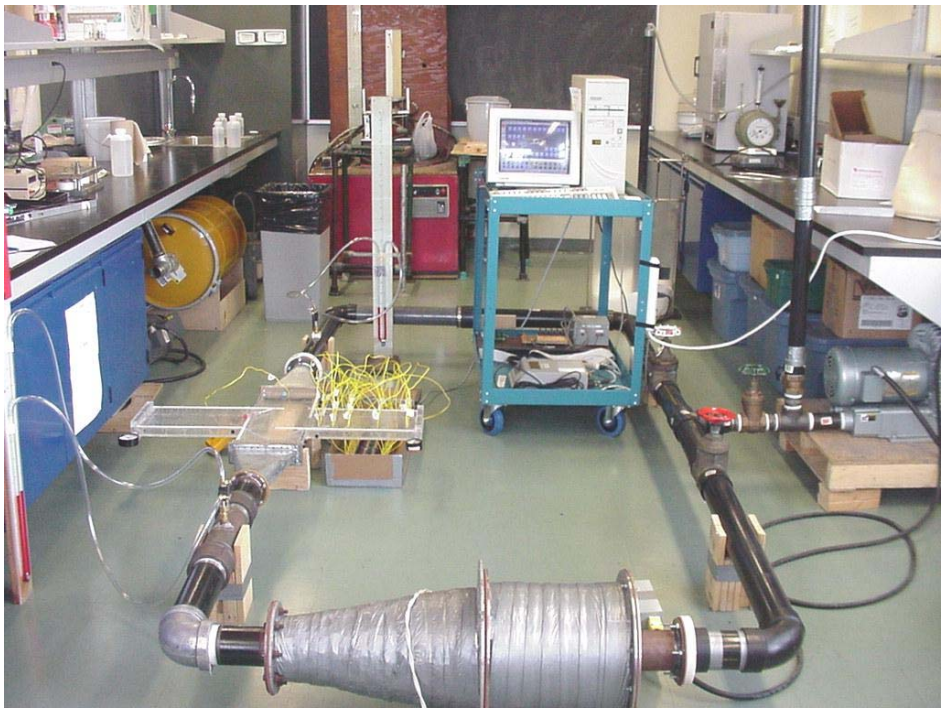

Figure 4.1d. A photograph of the overall heat transfer experimental set-up

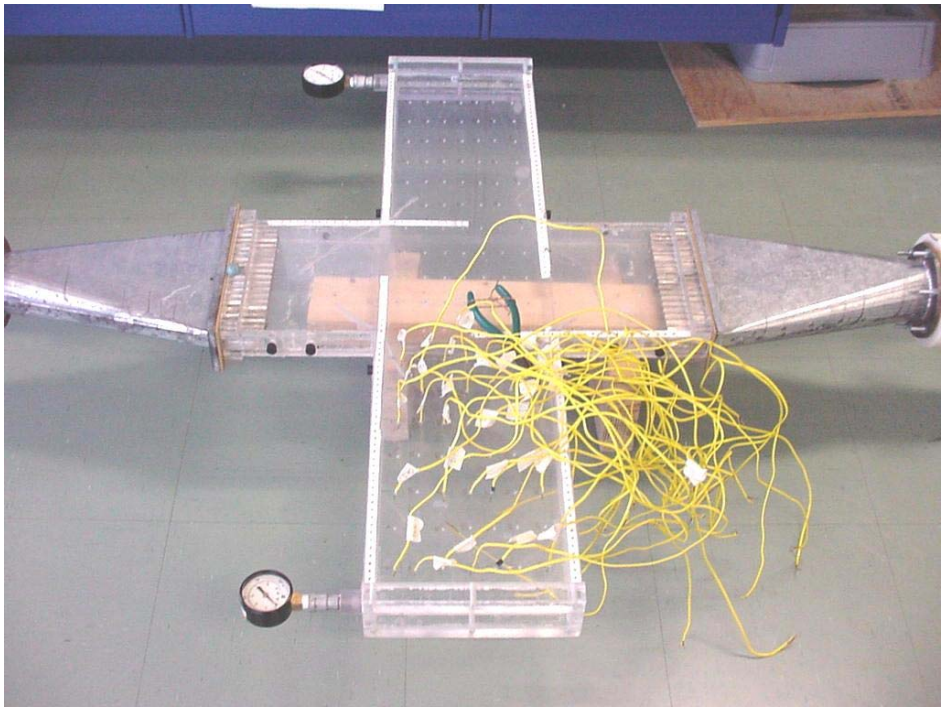

Figure 4.1e. A photograph of the IS used in the heat transfer experiments

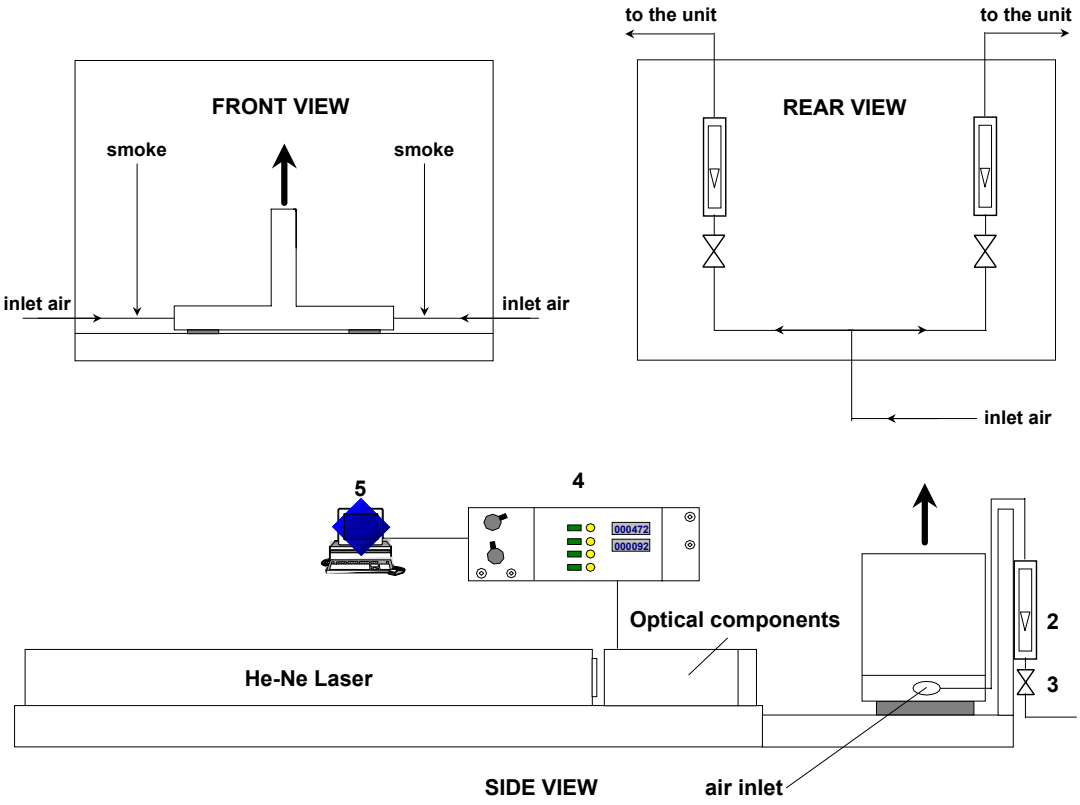

Figure 4.2a. A schematic diagram of the overall flow experimental set-up
1: one-way exit IS; 2: in-line rotameters; 3: gate valves; 4: signal processor; 5: computer

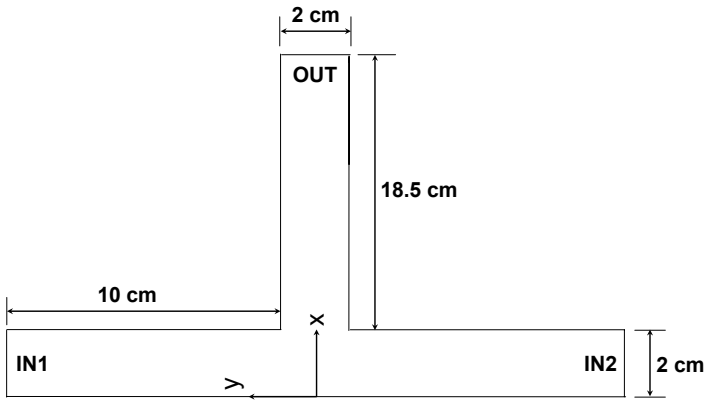

Figure 4.2b. Detailed diagram of the IS used in the flow experiments

A schematic diagram of the flow experimental set-up is shown in Figure 4.2a. Air was supplied to the IS through a compressed air line and the flowrate in each flow branch was controlled by a gate valve. The air flowrate in each flow branch was measured using an in-line rotameter (model no. FL-515, Omega Engineering, Inc., Stamford, CT).

The air streams were fed into a one-way exit IS through the two inlets (see Figure 4.2b). The two streams impinged normally against each other and left the IS through the exit. Velocity and turbulence intensity distributions in the IS were measured using a laser Doppler velocimeter (LDV) operated in the back-scattering mode. The system consisted of a 60 mW He-Ne laser (model no. 127, Spectra-Physics, Mountain View, CA), transmission optics with a beam splitter (model no. 9115-2, TSI, Inc., St. Paul, MN), a receiving assembly (model no. 9140, TSI, Inc., St. Paul, MN) with photomultiplier (model no. 9162, TSI, Inc., St. Paul, MN), which its power was supplied by a power supply (model no. 9165, TSI, Inc., St. Paul, MN). The focusing lens (model no. 9167-250, TSI, Inc., St. Paul, MN) used has a nominal focal length of 250 mm. An IS unit was mounted on a table with a traversing mechanism allowing measurements to be taken in the x and y directions. Smoke was introduced to the inlet air streams to provide seeding for the LDV. The signal obtained as particles suspended in the flow traversed the measuring field was processed by a signal processor (model no. 1990, TSI, Inc., St. Paul, MN). The processed signal was then transmitted to the computer for the final velocity and turbulence intensity computation using the software LDA Acquisition, version 1.0 (Plasma Technology Research Centre, Montreal, QC). At each measuring location the velocity and turbulence intensity were calculated by averaging the measurements of 2000 particles.

Photographs of the overall flow experimental set-up are shown in Figures 4.2c and 4.2d. A photograph of electronic components (signal processor, computer) of an LDV is shown in Figure 4.2e.

Since the fluid was confined, the laser beams must pass through a window of an IS before focusing. This window caused a deflection of the beams and a change in both the measuring volume location and the intersection angle of the two beams (TSI, 1980).

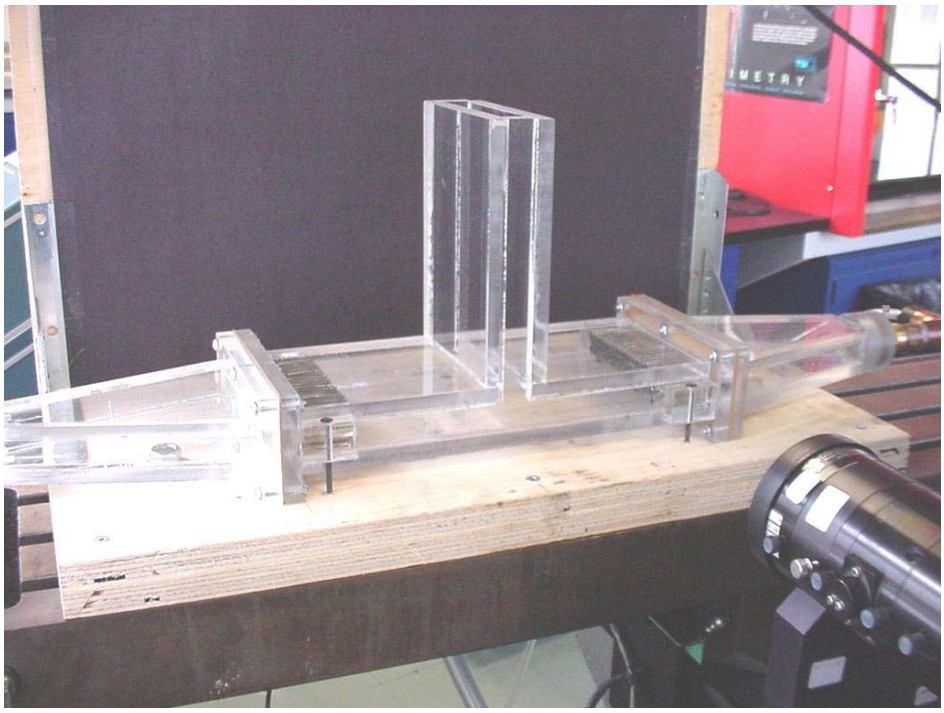

Figure 4.2c. A photograph of the overall flow experimental set-up (front view)

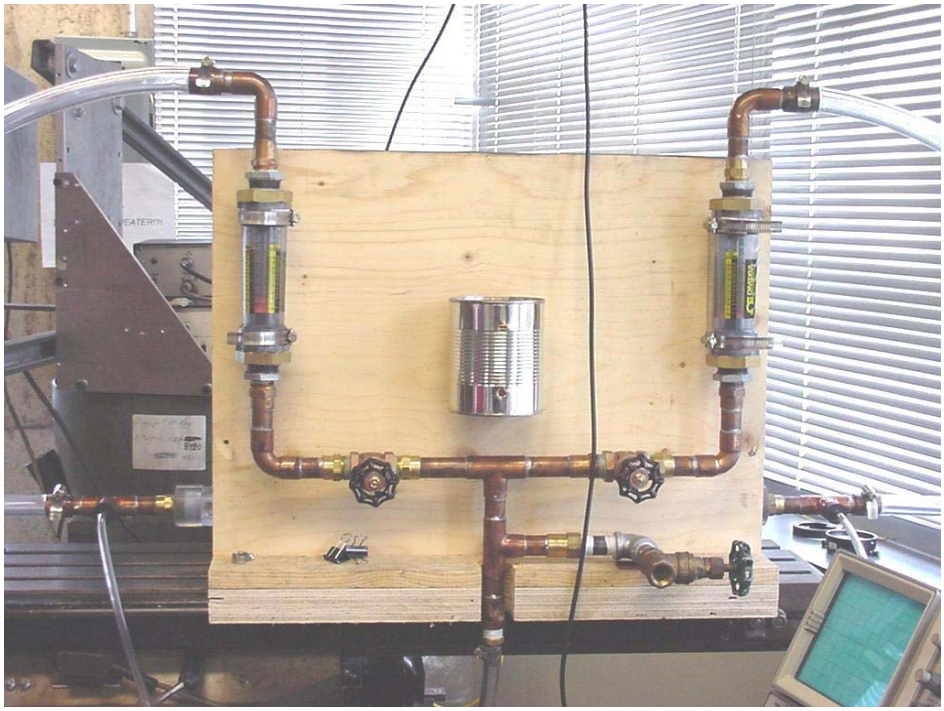

Figure 4.2d. A photograph of the overall flow experimental set-up (rear view)

Figure 4.2e. A photograph of electronic components of an LDV

A new focal distance, F, is calculated from the following equation:

$$F = F_D + t\left(1 - \frac{\tan\kappa_w}{\tan\kappa_f}\right) \tag{4.1}$$

where F is the actual focal distance, F_D is a given focal distance of lens, t is the thickness of the window. κ_w, the angle the beam within the window makes with the optical axis, is calculated from:

$$\kappa_w = \sin^{-1}\left(\frac{N_A \sin\kappa_A}{N_w}\right) \tag{4.2}$$

where N_A is the refractive index of the medium between the transmitting lens and the window, which equals to unity in the case of air. N_w is the refractive index of the window, which equals to 1.49 for Plexiglas used in the present study. For the case of air $\kappa_f = \kappa_A$, where κ_A is half angle of lens.

In addition to the above correction a lens mask (Figure 4.2f) was used to reduce beam reflections from the measuring window to enter the receiving optics.

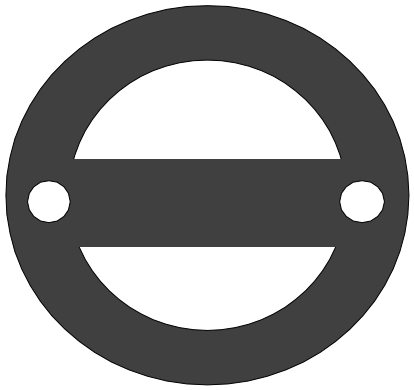

Figure 4.2f. A lens mask used in the flow experiments

To test the reproducibility of the data, replicates were made of randomly selected experiments. From these tests the reproducibility values for the temperature and velocity (as well as turbulence intensity) were within ± 4.7 and 3.3%, respectively.

4.3. MATHEMATICAL FORMULATION

To formulate the mathematical description of the transport processes in impinging streams the following assumptions are made: the mean flow is steady, incompressible and the fluid is Newtonian with constant physical properties. Viscous dissipation is neglected. The flow is assumed to be fully developed (both hydrodynamically and thermally) at the exit of the IS.

Based on the aforementioned assumptions the time-averaged conservation equations for mass, momentum and energy (in tensor form) can be written as follows:

Continuity equation:

$$\frac{\partial U_i}{\partial x_i} \tag{4.3}$$

Momentum equation:

$$\rho\left(U_i\frac{\partial U_j}{\partial x_i}\right)=-\frac{\partial P}{\partial x_j}+\frac{\partial}{\partial x_i}\left[\mu\left(\frac{\partial U_i}{\partial x_j}+\frac{\partial U_j}{\partial x_i}\right)-\rho\overline{u_i'u_j'}\right] \tag{4.4}$$

Energy equation:

$$\rho c_p\left(U_i\frac{\partial T}{\partial x_i}\right)=\frac{\partial}{\partial x_i}\left[k\frac{\partial T}{\partial x_i}-\rho\overline{u_i'T'}\right] \tag{4.5}$$

Reynolds stresses and turbulent heat flux are expressed as follows:

$$-\rho\overline{u_i'u_j'}=\mu_t\left(\frac{\partial U_i}{\partial x_j}+\frac{\partial U_j}{\partial x_i}\right)-\frac{2}{3}\rho k\delta_{ij} \tag{4.6}$$

$$-\rho\overline{u_i'T'}=\frac{\mu_t}{\sigma_T}\frac{\partial T}{\partial x_i} \tag{4.7}$$

The first ingredient of the composite turbulence model is a low-Reynolds number version of the k-ε model proposed by Lam and Bremhorst (1981). This model has been chosen based on the study of impingement heat transfer of Seyedein et al. (1994). In their work the Lam-Bremhorst (hereafter denoted by LB) model was shown to predict the heat transfer coefficient distributions very satisfactorily compared to other turbulence models tested.

In the LB model the turbulence kinetic energy and the isotropic component of the turbulence energy dissipation rate are determined from the following transport equations (Lam and Bremhorst, 1981):

$$\frac{\partial(\rho k)}{\partial t}+\frac{\partial(\rho U_i k)}{\partial x_i}=\frac{\partial}{\partial x_i}\left[\left(\frac{\mu_t}{\sigma_k}+\mu\right)\frac{\partial k}{\partial x_i}\right]+\mu_t\left(\frac{\partial U_i}{\partial x_j}+\frac{\partial U_j}{\partial x_i}\right)\frac{\partial U_i}{\partial x_j}-\rho\varepsilon \tag{4.8}$$

$$\frac{\partial(\rho\varepsilon)}{\partial t}+\frac{\partial(\rho U_i\varepsilon)}{\partial x_i}=\frac{\partial}{\partial x_i}\left[\left(\frac{\mu_t}{\sigma_\varepsilon}+\mu\right)\frac{\partial\varepsilon}{\partial x_i}\right]+C_1 f_1\mu_t\frac{\varepsilon}{k}\left(\frac{\partial U_i}{\partial x_j}+\frac{\partial U_j}{\partial x_i}\right)\frac{\partial U_i}{\partial x_j}-C_2 f_2\frac{\varepsilon^2}{k} \tag{4.9}$$

where $C_\mu=0.09$; $\sigma_k=1.00$; $\sigma_\varepsilon=1.314$; $C_1=1.44$ and $C_2=1.92$.

The wall-damping functions f_1, f_2 and f_μ are defined as follows:

$$f_1=\left(1+\frac{0.05}{f_\mu}\right)^3 \tag{4.10}$$

$$f_2=1-\exp(-R_t^2) \tag{4.11}$$

$$f_\mu = \left[1-\exp\left(-0.0165R_y\right)\right]^2\left(1+\frac{20.5}{R_t}\right) \tag{4.12}$$

where $R_t = \dfrac{\rho k^2}{\mu\varepsilon}$ and $R_y = \dfrac{\rho y k^{1/2}}{\mu}$.

As quoted by Hosseinalipour and Mujumdar (1995) there exists a secondary source/sink term in the ε equation that is taken as zero in most studies. This leads to an underestimation of near-wall ε values, which can cause an overestimation of the predicted heat transfer rate in separated flows. An example of this overestimation of heat transfer will be given in the subsequent section. Yap (1987) proposed the use of the following secondary source term:

$$S_\varepsilon = \max\left[0.83\left(\frac{l}{l_e}-1\right)\left(\frac{l}{l_e}\right)^2\frac{\varepsilon^2}{k},0\right] \tag{4.13}$$

where l_e denotes near-wall equilibrium length scale taken as 2.5 times the distance from the wall, while l, turbulence length scale, is defined as:

$$l \equiv \frac{k^{3/2}}{\varepsilon} \tag{4.14}$$

Finally, the time-averaged flow field can be determined using the turbulent viscosity modified by multiplication by a factor, which is a function of the local Reynolds number of turbulence (CHAM, 1997):

$$\mu_{\text{mod}} = \mu_t \cdot \min\left[1.0,\left(A\cdot R_t\right)^B\right] \tag{4.15}$$

$$\mu_t = \rho C_\mu f_\mu \frac{k^2}{\varepsilon} \tag{4.16}$$

where μ_{mod} is the turbulent viscosity to be used and μ_t is the nominal (high-Reynolds-number) value of μ_{mod}. A, B are constants in which the values, obtained in the present study by fitting numerical results to experimental impingement heat transfer data, equal to 0.05 and 2.40, respectively.

To ensure adequate concentration of grid cells near the wall the values of dimensionless distance of the first grid points normal to the wall, y^+, were always kept lower than unity.

Boundary conditions

To save computer time only half of the IS was simulated in all cases. In the following paragraphs W is the width of the inlet channels; H and L are the height and the length of the exit (or main flow) channels, respectively. The coordinates used are shown in Figure 4.1b. For parametric study H is fixed at H = 1 cm.

Inlet 1

$(0<x<W/2;\ y = W+H/2)$ $\quad U_1 = 0;\ U_2 = -U_{2,jet}$ and $T = T_{inlet\ 1}$ (4.17)

Inlet 2

$(0<x<W/2;\ y = -(W+H/2))$ $\quad U_1 = 0;\ U_2 = U_{2,jet}$ and $T = T_{inlet\ 2}$ (4.18)

and $k = \left(U_{jet} I\right)^2;\ \varepsilon = C_\mu^{3/4} \dfrac{k^{3/2}}{l}$ where $l = 0.1L$ and L is the characteristic length of the system; I represents the turbulence intensity.

Top and bottom walls

$(W/2<x<L+W/2)$ $\quad u_i = 0$ and $\dfrac{\partial T}{\partial y} = 0;\ k = 0$ and $\dfrac{\partial \varepsilon}{\partial y} = 0$ (4.19)

Outlet

$(x = L+W/2)$ $\quad \dfrac{\partial \phi}{\partial x} = 0$ (4.20)

where ϕ represents all solved variables.

The conservation equations, along with the boundary conditions, were solved numerically using the control-volume-based computational fluid dynamic software PHOENICS version 2.2.2 (CHAM, 1997). In this code the convection terms in the conservation equations were discretized using the hybrid scheme (Patankar, 1980). The discretized equations were solved using the well-known SIMPLEST algorithm (CHAM, 1997). The solution was considered converged when the following criterion is met for all the dependent variables:

$$\max \left| \frac{\phi^{n+1} - \phi^{n}}{\phi_r} \right| \leq 10^{-3} \tag{4.21}$$

between sweeps n and n+1; ϕ_r represents the reference value for the dependent variable ϕ. To improve convergence underrelaxation of the false transient type was used for the two velocity components and temperature. Linear relaxation was used for the pressure as

well as the turbulence kinetic energy and its dissipation rate. Whole-field residuals were checked to ensure that the converged solution set satisfies the governing equations within a prescribed error.

Due to the large number of cases studied it was not possible to check the grid independence for each individual case. To overcome this problem, as suggested by Hosseinalipour and Mujumdar (1997a), the appropriate number of grids were found through a grid doubling procedure for the "worst" case with the highest Reynolds number for each geometry and applied to all other cases for that particular geometry. This procedure results in longer running times for the lower Reynolds number cases but it was compensated for by the time saving in not running grid doubling runs for each individual case. For details regarding the discretization of the governing equations and various schemes used to solve the discretized equations the reader may refer to Patankar (1980).

4.4. RESULTS AND DISCUSSION

The composite model was first verified by comparing the predicted results with experimental impingement heat transfer data of van Heiningen (1982). The system configuration is shown in Figure 4.3. Flat velocity profile was used at the nozzle exit. The temperature of the confinement surface was kept equal to the temperature of the incoming jet while the temperature of the impingement surface was kept at some higher value. Local Nusselt number is calculated as:

$$Nu_x = \frac{(T_{imp} - T_{px})}{(T_{imp} - T_j)} \cdot \frac{W}{y_{px}} \tag{4.22}$$

The comparison between experimental results and numerical results obtained with the LB, LB with Yap correction (hereafter denoted by LBY) and composite models is shown in Figure 4.4. Grids of 80×70 nodes were used in all computations.

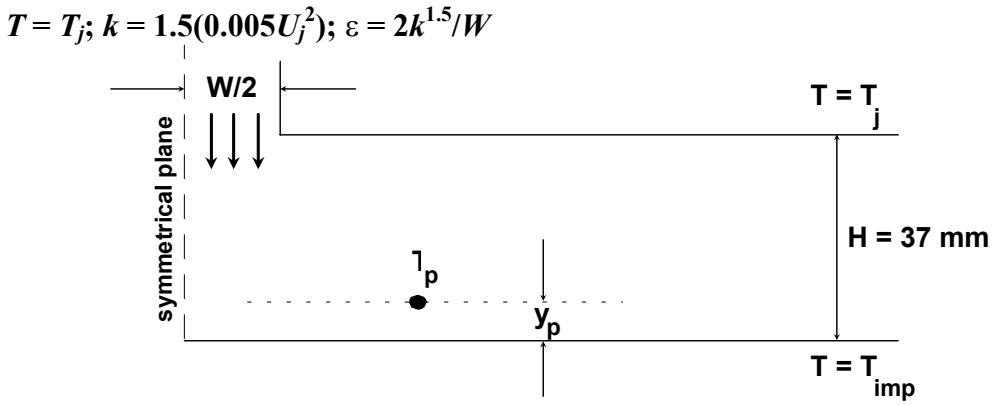

Figure 4.3. Impinging jet configuration used in model verification. *P* = near-wall node

It can be seen in Figure 4.4a that the LB model overestimates the values of Nusselt numbers at both stagnation point and points located downstream. This model predicts the shape of the Nusselt number profiles quite adequately, however. By applying Yap correction to the LB model, the overestimation of the stagnation Nusselt number decreases. However, the LBY model fails to capture the variation of local Nusselt numbers in the range $5 < x/W < 20$. By using the composite model, the stagnation Nusselt number is predicted well and the variation of the local heat transfer coefficients is also described well. Numerical results are also compared with experimental results in Figure 4.4b for another set of operating and geometric parameters. In this figure the LBY model performs similarly to the composite model since the profiles vary smoother along the impingement surface in this case than the one presented in Figure 4.4a.

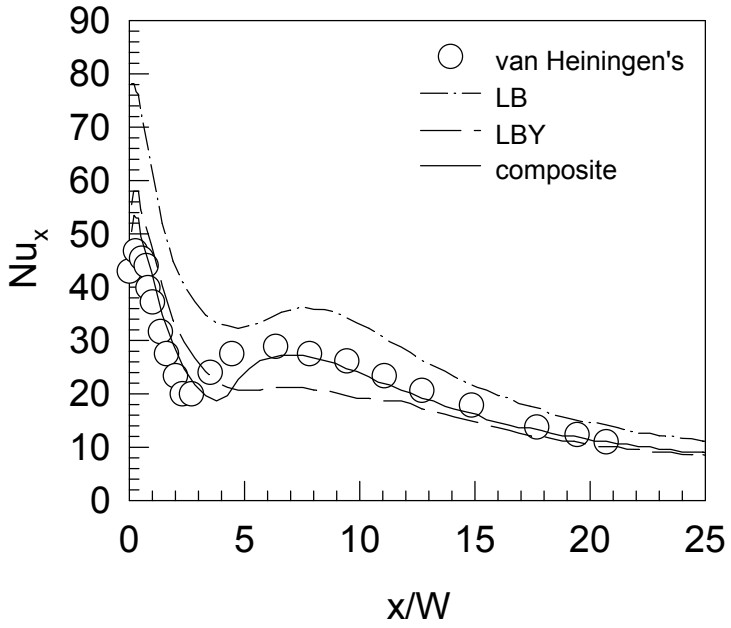

Figure 4.4a. Comparison between predicted and experimental local Nusselt number profiles along the impingement surface. Re_j = 10400; H/W = 2.6

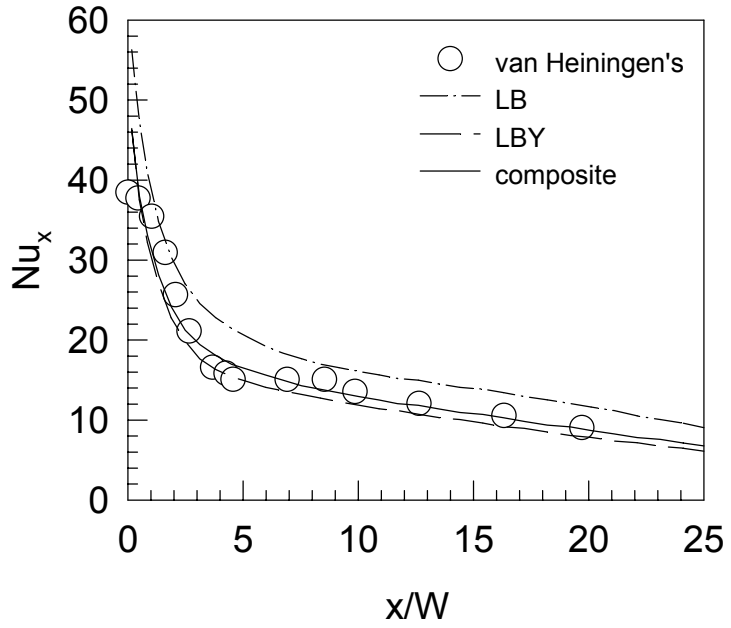

Figure 4.4b. Comparison between predicted and experimental local Nusselt number profiles along the impingement surface. Re_j = 5200; H/W = 6.0

The comparison between normalized numerical and experimental temperature profiles in IS is shown in Figure 4.5. Grids of 100×80 nodes provide adequate resolution in these cases. The computational domain was extended long enough in the downstream direction to satisfy the fully developed flow assumption at the exits of the IS. Temperatures were measured at 5 different x-locations, i.e., at x = 15, 20, 25, 35 and 45 cm from the origin of the x-coordinate (see Figure 4.1c). Temperature values are normalized with the reference temperatures of 30^o and 40^o C when the temperature difference between the hot and cold streams is 10^o and 20^o C, respectively. Inlet jet turbulence intensity was assumed to be $I = 2\%$.

At each measuring location the value of the reference temperature is taken as zero in terms of the modified x-coordinate (X); the difference between the actual and reference temperatures is then plotted with the scale of 0.1 cm per 1^o C. For example, in Figure 4.5a, at x = 15 cm and y = 5 cm, the actual temperature is 42.3^o C and the reference temperature is 40^oC. The modified x-coordinate of this point on the graph is then $X = 15 + ((42.3\text{-}40) \times 0.1) = 15.23$ cm.

It can be seen from Figures 4.5a and 4.5b that the composite model predicts the temperature profiles very similarly to those predicted by LB and LBY models. This is not unexpected since the mean flow properties (e.g., temperature profiles) are normally not as much affected by the choice of the turbulence model as the near-wall quantities and their gradients (e.g., heat flux) are. Also, turbulent viscosity (and hence turbulent Prandtl number) variations cannot explain the 100% error of the standard k-ε model (Behnia et al., 1999). The maximum deviation of about 25% between numerical and experimental results observed in the upper left corner of Figure 4.5a may be attributed also to the simplifying assumption of constant physical fluid properties as well as the implicit assumption of adiabatic wall condition in the simulation; the model predicts the results well within $\pm 5\%$ in the lower left region where the inlet temperature was lower (and hence less heat loss through the wall). The model performs better as the fluid approaches the outlet, as expected. It is important to note, however, that the composite model gives much faster convergence than do the LB and LBY models. The model also captures well the location of impingement planes as it is pushed towards the weaker jet in Figure 4.5b (compared to being more or less at the middle of the channel in Figure 4.5a).

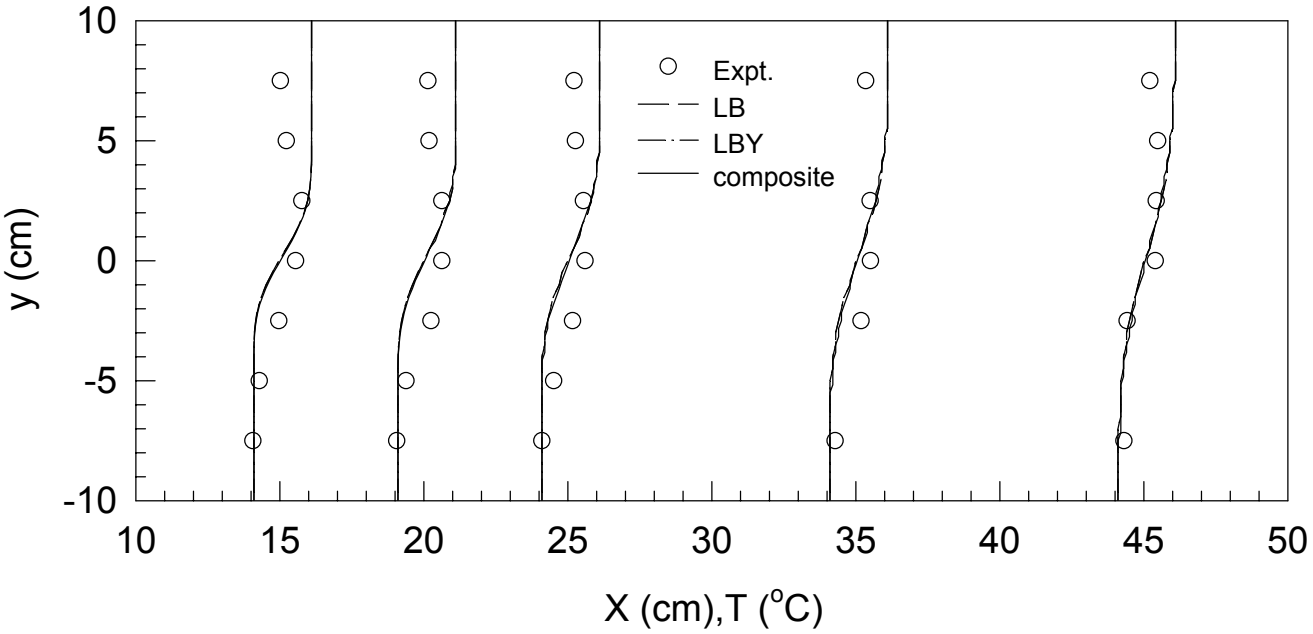

(a) Re_j = 18000 (top)-18000 (bottom); I = 2%; ΔT = 20° C (51° C/31° C); normalized T = 40° C

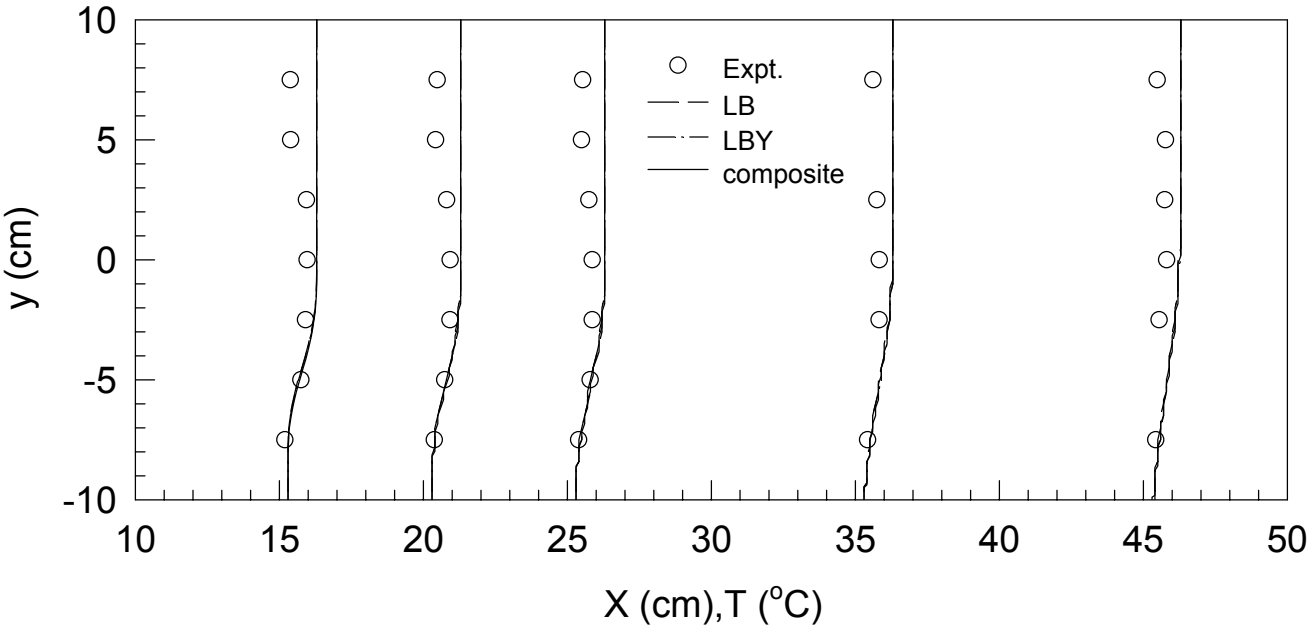

(b) Re_j = 20000 (top – hot stream) - 10000 (bottom – cold stream); I = 2%; ΔT = 10° C (43° C/33° C); normalized T = 30° C

Figure 4.5. Comparison between predicted and experimental normalized temperature profiles in IS

The comparison between normalized numerical and experimental velocity profiles in a one-way exit IS is shown in Figure 4.6a. Grids of 110×60 nodes provide adequate resolution in these cases. The computational domain was again extended long enough in the downstream direction to satisfy the fully developed flow assumption at the exit of the IS. Velocities were measured at 5 different x-locations, i.e., at x = 3.5, 7.5, 11.5, 15.5 and 19.5 cm from the origin of the x-coordinate in Figure 4.2b. The velocity values are normalized with the zero reference velocity. The same calculation procedure as used in the temperature case applies; the difference between the actual and reference velocities is plotted, in this case, with the scale of 0.3 cm per 1m s^{-1}.

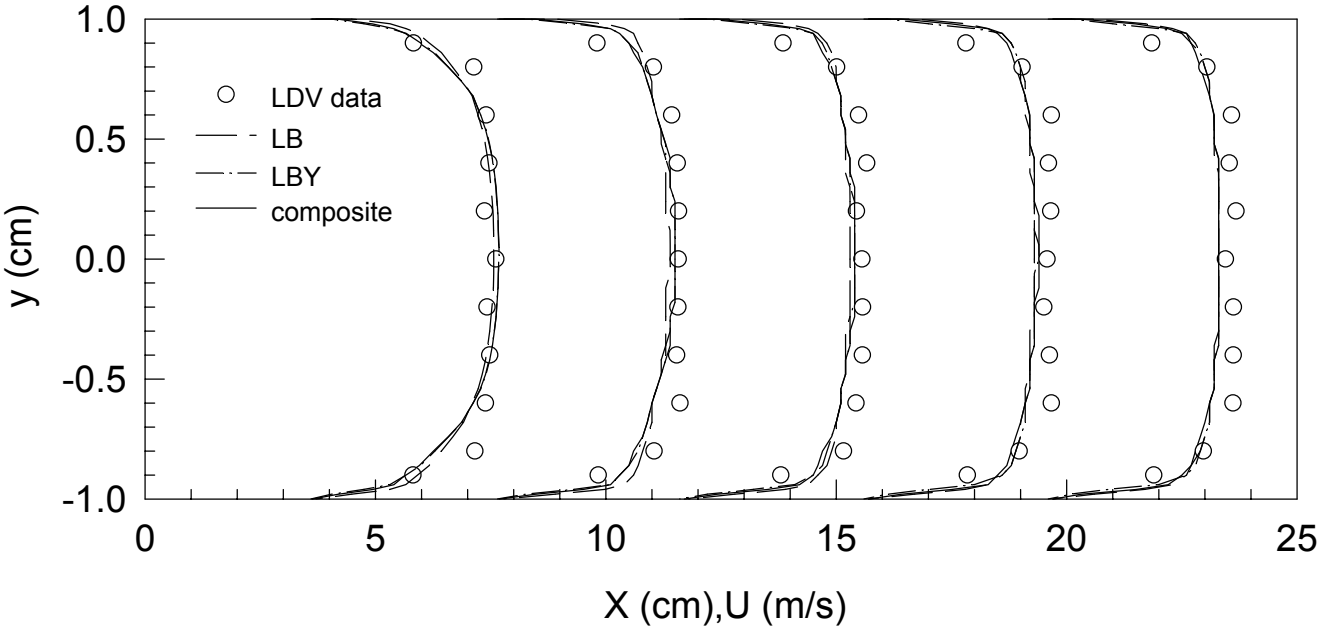

Figure 4.6a. Comparison between predicted and experimental normalized velocity profiles in IS. Re_j = 12600; I = 15%; normalized U = 0 m s^{-1}

Figure 4.6a compares the LDV measurements of the axial mean velocity with the numerical results predicted by the LB, LBY and composite models. It can be seen from this figure that the composite model performs slightly better than the LB model but gives no appreciably different results from the LBY model. The model overestimates the velocity in the near-wall region (up to about 20%) but slightly underestimates

(approximately 7%) it in the region far away from the wall. It should be noted, however, that the near-wall measurements are also subjected to higher errors due to the reflection of the laser light from the edge of the model IS used in the experiments. Nevertheless, this confirms the usability of the composite model, especially when taking into account the fact that convergence is much faster with this model than the other two models tested here.

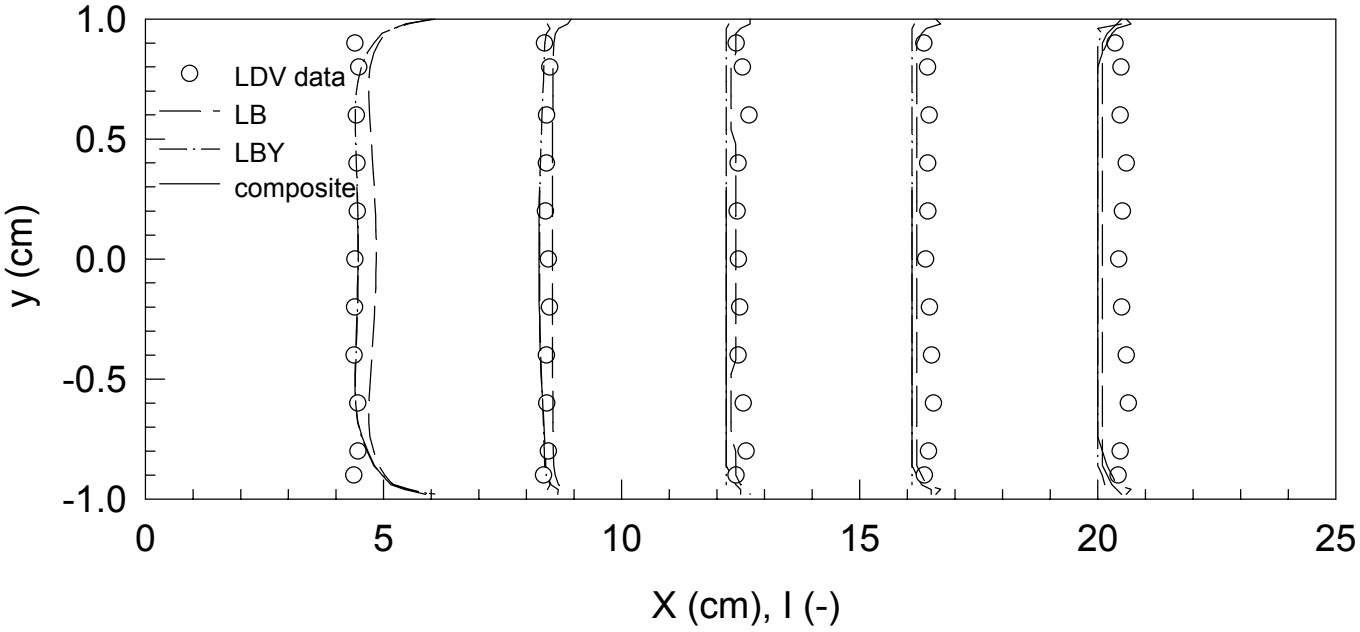

Figure 4.6b. Comparison between predicted and experimental normalized turbulence intensity profiles in IS. Re_j = 12600; I = 15%; normalized I = 0%

The comparison between normalized numerical and experimental turbulence intensity profiles in a one-way exit IS is shown in Figure 4.6b. The measuring locations and computational grid density are the same as the one used for the velocity measurements and calculation. The turbulence intensity values are normalized with the zero reference intensity. The difference between the actual and reference intensities is plotted, in this case, with the scale of 5 cm per I.

It can be seen from this figure that the composite model predicts the distribution of I better than does the LB model, especially in the area not so far downstream of the impingement region. The overestimation of I (hence the turbulence kinetic energy) by the LB model is due to the omission of the secondary source/sink term in the ε equation mentioned earlier. Further downstream, however, the two models seem to give no appreciably different results. The composite model predicts the intensity profiles very similarly to the LBY but convergence is again much faster. Again, the model overestimates the intensity in the near-wall region but underestimates it in the region far away from the wall. The implicit assumption of isotropy in the model also will affect the results. Unfortunately, it was not possible with the instrumentation available to measure the three components of the turbulence intensity.

Temperature was used as a passive tracer to monitor mixing of the two fluid streams. As the two streams mix and approach the exit ports the temperature profiles across the exit channel height are flattened; the well-mixed condition is satisfied when no temperature gradient exists across the channel height, i.e., the temperature profile is flat. To quantify the mixing performance of the system at different operating conditions and geometric configurations a mixing index was defined as follows:

$$\text{Mixing index} = \frac{\sigma_T}{\Delta T} \tag{4.23}$$

where σ_T is the standard deviation of the fluid temperature across the channel height at a specific axial location and ΔT is the temperature difference between the two inlet streams. $\sigma_T = 0$ thus implies well-mixed condition. Note that different criteria for mixing (e.g., the one proposed by Hosseinalipour and Mujumdar (1997a)) may be used but the above criterion is conceptually easier to visualize. Nonetheless, either index should equally predict the channel length required to well mix the two streams. The ranges of parameters studied are: inlet jet Reynolds number (Re_j) from 10000 to 30000; inlet jet turbulence intensity (I) from 1 to 2%; the ratio of the height of the exit channel to the width of the inlet jet (H/W) was varied from 1.0 to 2.0. Inlet jet hydraulic diameter is calculated assuming the aspect ratio of 5 between the width and the height of the exit channel.

The plots of the mixing index versus dimensionless axial distance with the inlet jet Reynolds number as a parameter are shown in Figures 4.7a-4.7d. Both dimensional

and dimensionless coordinates are shown in these figures for easy comparison. Grids of 155×62 nodes were used in all computations.

It can be seen from these figures that as the jet Reynolds number increases mixing is improved until some specific values of *x/W* are reached. These critical values depend on both the operating conditions as well as the geometry of the system. This behavior is quite different from what is observed in laminar IS of similar geometries (see Chapter 3). For the same *H/W* laminar IS mixing is always poorer as Re_j increases due to the increase in mean flow rate of the fluid in the system (and hence shorter residence time of the fluid in the system). For turbulent IS increasing Re_j leads to higher levels of the turbulence kinetic energy, especially in the impingement zone. The values of the turbulent viscosity are also higher at higher Re_j; this increase leads to a stronger eddy mixing. Once the critical value of *x/W* is reached, however, the mixing behavior is reversed. This may be ascribed to the already mentioned increased mean flow rate; the effect of higher turbulence kinetic energy at higher Re_j is overshadowed by the effectively shorter transit time.

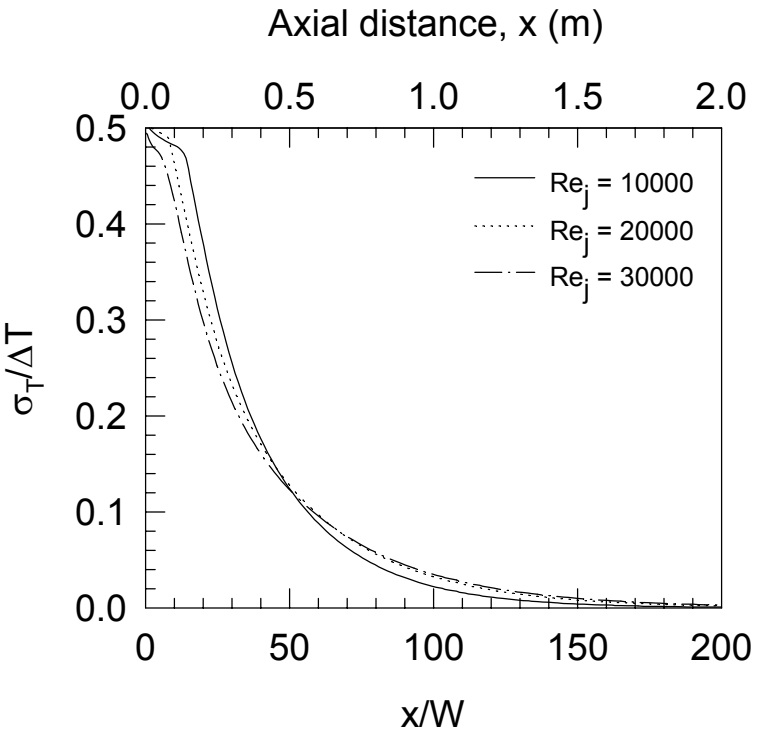

Figure 4.7a. Mixing index for *H/W* = 1.0; *I* = 1%

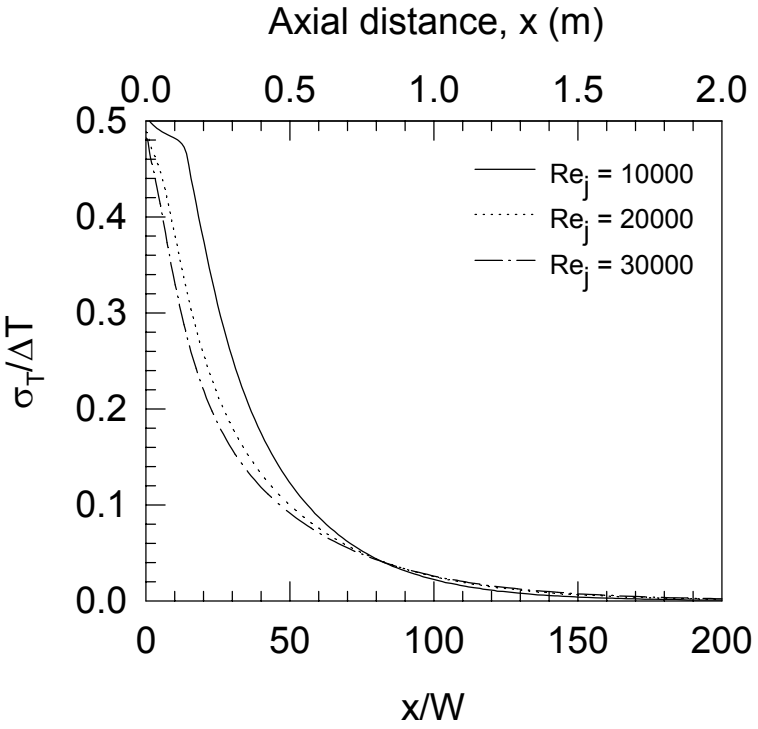

Figure 4.7b. Mixing index for $H/W = 1.0$; $I = 2\%$

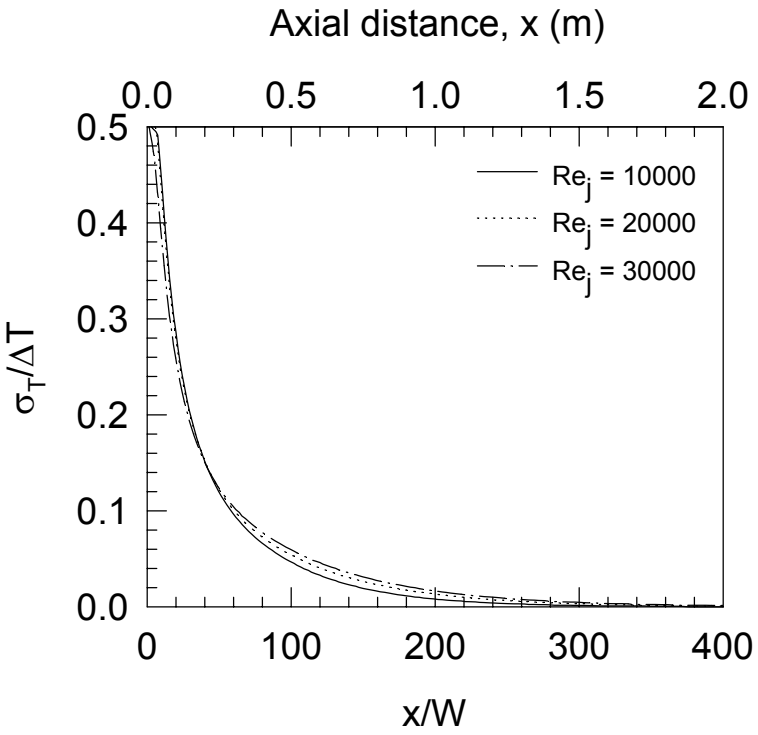

Figure 4.7c. Mixing index for $H/W = 2.0$; $I = 1\%$

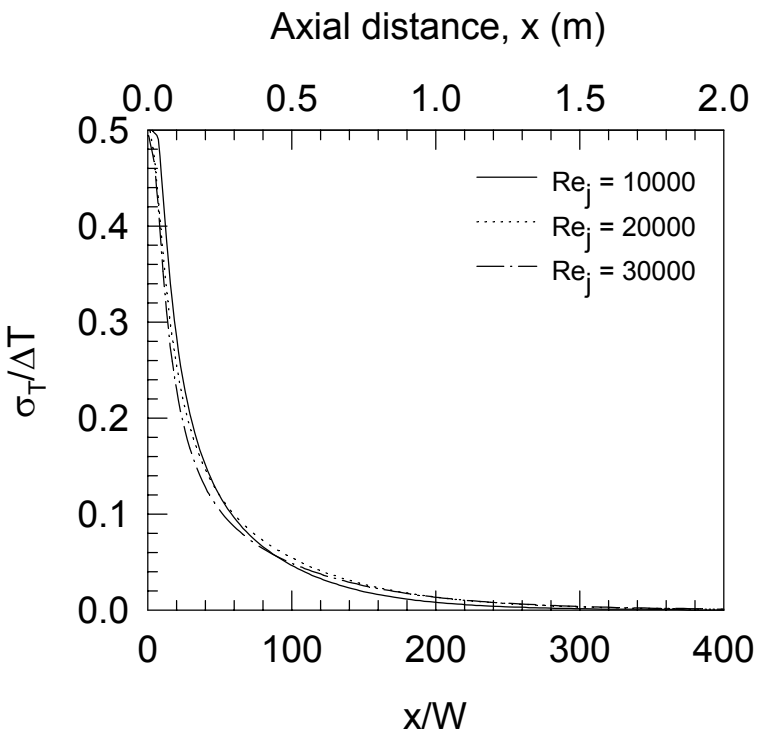

Figure 4.7d. Mixing index for $H/W = 2.0$; $I = 2\%$

Increasing H/W results in smaller effect of Re_j on the mixing in IS at low x/W values (i.e., before the critical x/W is reached). The effect is more pronounced at higher inlet jet turbulence intensities. This again is due to the increased eddy mixing as mentioned earlier. Increasing the turbulence intensity also increases the critical value of x/W where the mixing behavior is reversed as more turbulence energy is generated resulting in better mixing.

Figure 4.8 gives an example of the effect of the system geometry on mixing in IS. For each Re_j and turbulence intensity increasing *H/W* leads to better mixing at low *x/W* values but poorer mixing at *x/W* values beyond the critical value. For the same Re_j the jet velocity is higher in the case of IS with higher *H/W* due to the smaller jet opening (*H* is fixed at a constant value). This leads to higher turbulent viscosity and hence better eddy mixing. However, as the jet velocity increases the lateral component of momentum tends to push the fluid out of the system faster. The fluids thus have lesser time in the system to mix.

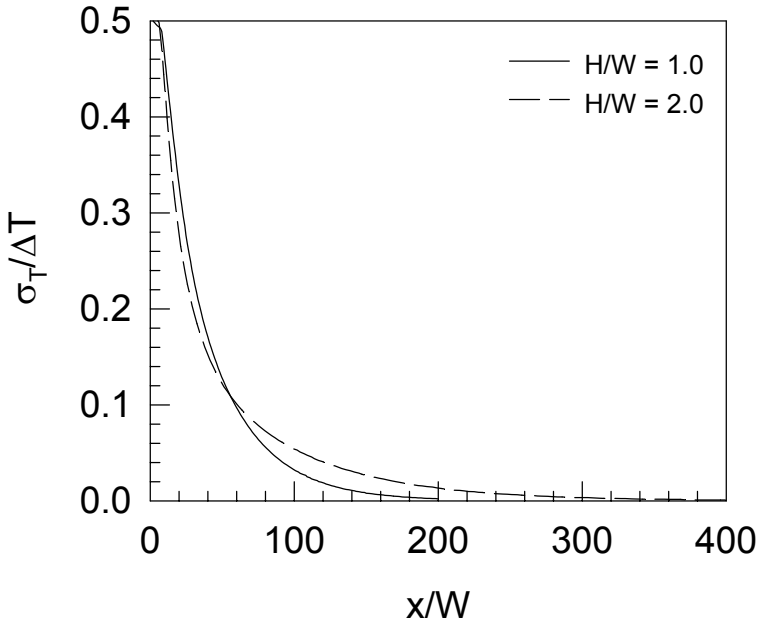

Figure 4.8. Mixing index for Re_j = 20000; *I* = 1%

The effect of inlet jet turbulence intensity is shown in Figure 4.9 for Re_j = 20000. For the case with Re_j = 10000 there is no difference between *I* = 1 or 2%. The inlet jet velocity (in combination with the turbulence intensity) may not be high enough to yield any difference in the turbulence energy and turbulent viscosity to make any difference in the mixing. The characteristics of the mixing curves for the cases with Re_j = 20000 and 30000 are very similar. It can be seen in this figure that increased turbulence intensity leads to better mixing despite the small increase in the absolute turbulence kinetic energy.

The reason is as mentioned earlier. The difference in terms of the distance to attain well-mixed condition is not significant, however.

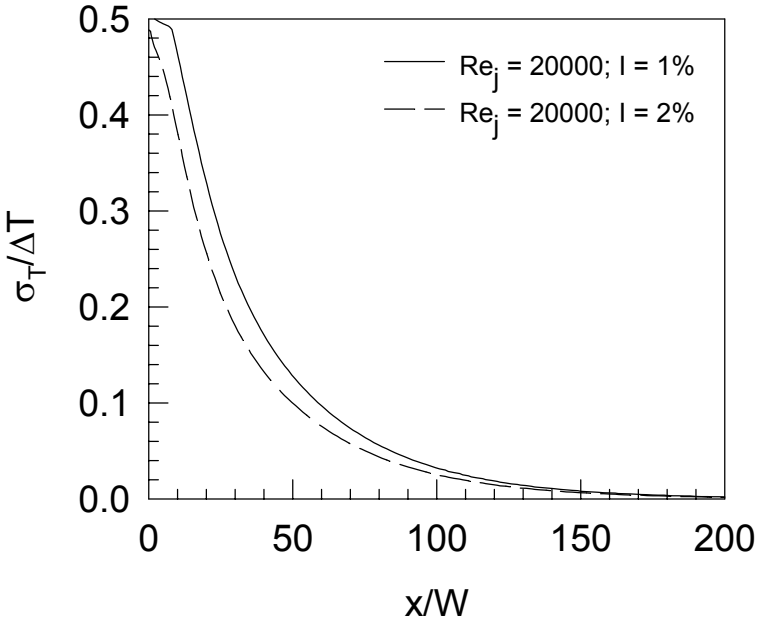

Figure 4.9. Mixing index for H/W = 1.0; Re_j = 20000

CLOSING REMARKS

A study was performed of the mixing characteristics of turbulent confined impinging streams. A new composite turbulence model is proposed and verified by comparing its predictions with available experimental impingement heat transfer data as well as the experimental temperature and velocity distributions in impinging streams obtained in the present work. The model is found to give better agreement between experimental and numerical impingement heat transfer results than two other low-Reynolds number k-ε turbulence models tested. The model was then used to perform a parametric study of mixing in a two-dimensional turbulent confined IS. It is found that, for each H/W, as the jet Reynolds number increases mixing is better until a critical value of x/W is reached beyond which the mixing behavior is reversed. This behavior is quite

different from that of two-dimensional laminar confined impinging streams reported in Chapter 3. Increasing *H/W* results in reduced effect of Re_j on mixing at low *x/W* values. The effect is more pronounced at higher inlet jet turbulence intensity particularly at high Re_j. For each Re_j and turbulence intensity increasing *H/W* leads to better mixing at low *x/W* values but poorer mixing at *x/W* values beyond the critical value. Good mixing is obtained over a rather short distance for all cases examined. To improve mixing even further two-stage IS may be used. Fluid can be drawn from the first stage at a selected location and fed into the second stage for additional mixing.

NOMENCLATURE

A, B, C_1	
C_2, C_μ	turbulence model constants, -
c_p	heat capacity, J kg^{-1} K^{-1}
D_h	inlet channel hydraulic diameter, m
f_1, f_2, f_μ	turbulence model functions, -
F	actual focal distance of lens, mm
F_D	given focal distance of lens, mm
H	height of the exit channel, m
I	turbulence intensity, %
k	thermal conductivity, W m^{-1} K^{-1} (equation (4.5))
k	turbulence kinetic energy, m^2 s^{-2}
l	turbulence length scale, m
l_e	near-wall equilibrium length scale, m
L	length of the exit channel, m
N_A	refractive index of the medium (between transmitting lens and window), -
N_w	refractive index of the window, -
P	time-averaged pressure, Pa
R_t	turbulence Reynolds number, $\frac{\rho k^2}{\mu\varepsilon}$, -

R_y	turbulence Reynolds number, $\frac{\rho y k^{1/2}}{\mu}$, -
t	time, s
t	thickness of the measuring window, mm
T	time-averaged temperature, ^{o}C
T'	fluctuating component of temperature, ^{o}C
ΔT	temperature difference of the two inlet streams, ^{o}C
u_i', u_j'	fluctuating velocity components, m s^{-1}
u_τ	friction velocity, $\sqrt{\tau_w / \rho}$, m s^{-1}
U_i, U_j	time-averaged velocity components, m s^{-1}
W	width of the inlet channel, m
x_i, x_j	coordinates, m
y^+	dimensionless distance from the wall, $\frac{u_\tau y \rho}{\mu}$, -

Greek letters

δ_{ij}	Kronecker delta, -
ε	isotropic turbulence dissipation rate, m^2 s^{-3}
κ_A	angle the incident beam makes with the optical axis (half angle of lens), ^{o}
κ_f	angle the beam within the fluid makes with the optical axis, ^{o}
κ_w	angle the beam within the window makes with the optical axis, ^{o}
μ	dynamic viscosity, kg m^{-1} s^{-1}
μ_t	turbulent viscosity, kg m^{-1} s^{-1}
ρ	density, kg m^{-3}
σ_T	standard deviation of temperature, ^{o}C
σ_k	diffusion Prandtl number for turbulence kinetic energy, -
σ_ε	diffusion Prandtl number for dissipation rate, -
σ_T	turbulent Prandtl number, -
τ_w	shear stress at the wall, kg m^{-1} s^{-2}

Subscripts

imp	impingement surface

j jet

p near-wall grid point

Dimensionless group

Re_j jet Reynolds number, $\frac{D_h U_{jet} \rho}{\mu}$

REFERENCES

Bauer, W., Haag, O., Hennecke, D.K., 2000, Accuracy and robustness of nonlinear eddy viscosity models, *International Journal of Heat and Fluid Flow*, 21, pp. 312-319.

Behnia, M., Parneix, S., Shabany, Y., Durbin, P.A., 1999, Numerical study of turbulent heat transfer in confined and unconfined impinging jets, *International Journal of Heat and Fluid Flow*, 20, pp. 1-9.

Berman, Y., Tamir, A., 1996, Experimental investigation of phosphate dust collection in impinging streams, *Canadian Journal of Chemical Engineering*, 74, pp. 817-821.

Berman, Y., Tamir, A., 2000, Extraction in thin liquid films generated by impinging streams, *AIChE Journal*, 46, pp. 769-778.

Berman, Y., Tanklevsky, A., Oren Y., Tamir, A., 2000a, Modeling and experimental studies of SO_2 absorption in coaxial cylinders with impinging streams, part I, *Chemical Engineering Science*, 55, pp. 1009-1021.

Berman, Y., Tanklevsky, A., Oren Y., Tamir, A., 2000b, Modeling and experimental studies of SO_2 absorption in coaxial cylinders with impinging streams, part II, *Chemical Engineering Science*, 55, pp. 1023-1028.

Concentration, Heat and Momentum Limited (CHAM), 1997, *POLIS: Phoenics On-Line Information System*, London, UK.

Hosseinalipour, S.M., Mujumdar, A.S., 1995, Comparative evaluation of different turbulence models for confined impinging and opposing jet flows, *Numerical Heat Transfer, Part A*, 28, pp. 647-666.

Hosseinalipour, S.M., Mujumdar, A.S., 1997a, Flow and thermal characteristics of steady two-dimensional confined laminar opposing jets: part I. equal jets, *International Communications in Heat and Mass Transfer*, 24, pp. 27-38.

Hosseinalipour, S.M., Mujumdar, A.S., 1997b, Flow and thermal characteristics of steady two-dimensional confined laminar opposing jets: part II. unequal jets, *International Communications in Heat and Mass Transfer*, 24, pp. 39-50.

Kitron, Y., Tamir, A., 1988, Performance of a coaxial gas-solid two-impinging-streams reactor: hydrodynamics, residence time distribution, and drying heat transfer, *Industrial & Engineering Chemistry Research*, 27, pp. 1760-1767.

Kudra, T., Mujumdar, A.S., 1989, Impinging stream dryers for particles and pastes, *Drying Technology – An International Journal*, 7, pp. 219-266.

Kudra, T., Mujumdar, A.S., 1995, Impinging stream dryers, pp. 539-566, in A.S. Mujumdar (Ed.) *Handbook of Industrial Drying, 2nd Edition*, Marcel Dekker, New York.

Lam, C.K.G., Bremhorst, K., 1981, A modified form of the k-ε model for predicting wall turbulence, *ASME Journal of Fluids Engineering*, 103, pp. 456-460.

Morris, G.K., Garimella, S.V., Amano, R.S., 1996, Prediction of jet impingement heat transfer using a hybrid wall treatment with different turbulent Prandtl number functions, *ASME Journal of Heat Transfer*, 118, pp. 562-569.

Patankar, S.V., 1980, *Numerical Heat Transfer and Fluid Flow*, Hemisphere, Washington.

Seyedein, S.H., Hasan, M., Mujumdar, A.S., 1994, Modelling of a single confined turbulent slot jet impingement using various k-ε turbulence models, *Applied Mathematical Modelling*, 18, pp. 526-537.

Sohrabi, M., Marvast, M.A., 2000, Application of a continuous two impinging streams reactor in solid-liquid enzyme reactions, *Industrial & Engineering Chemistry Research*, 39, pp. 1903-1910.

Tamir, A., 1994, *Impinging-Stream Reactors: Fundamentals and Applications*, Elsevier, Amsterdam.

TSI Incorporated, 1980, *Systems 9100-4 and 9100-5 Laser Doppler Velocimeters Instruction Manual*, St. Paul, MN.

Unger, D.R., Muzzio, F.J., Brodkey, R.S., 1998, Experimental and numerical characterization of viscous flow and mixing in an impinging jet contactor, *Canadian Journal of Chemical Engineering*, 76, pp. 546-555.

van Heiningen, A.R.P., 1982, Heat transfer under an impinging slot jet, Ph.D. Thesis, Department of Chemical Engineering, McGill University, Canada.

Yap, C.R., 1987, Turbulent heat and momentum transfer in recirculating and impinging flows, Ph.D. Thesis, Faculty of Technology, University of Manchester, UK (Quoted by Hosseinalipour and Mujumdar, 1995).